# Thermoelectric Transport in $Ru_2TiSi$ Full-Heusler Compounds

Fabian Garmroudi,[1,*] Michael Parzer,[1] Takao Mori,[2,3] Andrej Pustogow,[1] and Ernst Bauer[1]

[1] *Institute of Solid State Physics, TU Wien, 1040 Vienna, Austria*

[2] *International Center for Materials Nanoarchitectonics (WPI-MANA), National Institute for Materials Science, Tsukuba 305-0044, Japan*

[3] *University of Tsukuba, Tsukuba 305-8577, Japan*

(Received 3 December 2024; accepted 29 January 2025; published 3 March 2025)

Heusler compounds with six valence electrons per atom have attracted interest as thermoelectric materials owing to their semimetallic and semiconducting properties. Here, we theoretically and experimentally investigate electronic transport in $Ru_2TiSi$-based full-Heuslers. We show that electronic transport in this system can be well captured by a two-parabolic-band model. The larger band gap of $Ru_2TiSi$ promises a higher thermoelectric performance, compared to its isovalent family member $Fe_2VAl$, which has been studied as a thermoelectric material for over two decades. Additionally, we identify $p$-type $Ru_2TiSi$ as far more efficient than previously studied $n$-type compounds and demonstrate that this can be traced back to much lighter and more mobile holes originating from dispersive valence bands. Our findings suggest that an exceptionally high dimensionless figure of merit $zT > 1$ can be realized in these $p$-type compounds around 700 K upon proper reduction of the lattice thermal conductivity, e.g., by substituting Zr or Hf for Ti.

DOI: 10.1103/PRXEnergy.4.013010

## I. INTRODUCTION

Heusler compounds represent a highly tunable material platform encompassing over one thousand different members that exhibit a variety of interesting electronic phases, ranging from half-metallicity to semiconducting states and nontrivial topological band structures [1–3]. Heusler compounds are typically subcategorized into half-Heuslers (hHs) and full-Heuslers (fHs) with $XYZ$ and $X_2YZ$ stoichiometries, respectively. In hHs, crystallizing in the noncentrosymmetric $C1_b$ structure (space group no. 216, $F\bar{4}3m$), one of the $X$ sublattices is vacant, whereas the fH structure with $L2_1$ ordering (space group no. 225, $Fm\bar{3}m$) can be interpreted as four interpenetrating fcc sublattices, two of which are comprised of $X$ atoms, while the others are built up from the $Y$ and $Z$ atoms. The $X$ and $Y$ atoms are usually transition metals, whereas the $Z$ atom is typically a main-group-III, -IV, or even -V element [1].

In general, research on Heusler materials is guided by simple electron-counting rules, such as the Slater-Pauling rule [1,4–6], which states that Heusler compounds with an average valence electron concentration (VEC) of six valence electrons per atom are nonmagnetic semiconductors or semimetals, depending on the strength of hybridization. However, as the VEC increases or decreases, magnetic metals emerge. Although there are few exceptions to this [7,8], hundreds of hH and fH compounds align with this concept and researchers have adhered to these straightforward electron-counting rules, as they enable an accurate and quick estimate of the electronic- and magnetic-ground-state properties and serve as fundamental principles [1], particularly in the quest for thermoelectric semiconductors [9–12].

The performance of thermoelectric materials is evaluated by the dimensionless figure of merit $zT = S^2\sigma\kappa^{-1}T$, which depends on the Seebeck coefficient $S$, the electrical conductivity $\sigma$, the thermal conductivity $\kappa$, and the absolute temperature $T$, and directly determines the efficiency of a thermoelectric conversion device. For practical purposes, $zT > 1$ is commonly considered as a threshold [13]. While numerous hH compounds, e.g., (Ti,Zr,Hf)NiSn, (Nb,Ta)FeSb, etc., are already widely recognized as efficient thermoelectric materials [14–16], their fH relatives have not yet reached $zT$ values that would make them competitive with state-of-the-art materials [17].

$Fe_2VAl$ is unarguably the most prominent fH thermoelectric material, with attractive near-room-temperature thermoelectric properties [18–20]. Despite consisting only of metallic elements, $Fe_2VAl$ is a semimetal with a tiny

*Contact author: f.garmroudi@gmx.at

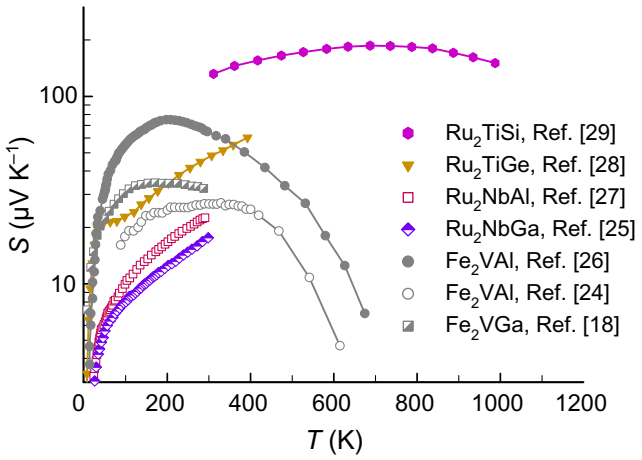


FIG. 1. A comparison of the temperature-dependent Seebeck coefficients of various semimetallic and semiconducting fHs with six valence electrons per atom [18,24–29].

band overlap or an almost gapless semiconductor [21–23]. There are two primary factors limiting the performance of $Fe_2VAl$ thermoelectrics: (i) their intrinsically large lattice thermal conductivity and (ii) the small band gap, which already results in bipolar conduction at $T \lesssim 300$ K. In Fig. 1, we compare the temperature-dependent Seebeck coefficient $S(T)$ of various fH compounds with an effective valence electron concentration of six valence electrons per atom, VEC = 6, reported and experimentally studied in the literature previously [18,24–29]. Note the pronounced maximum in $S(T)$ of $Fe_2VAl$ at around 200 K, arising from the aforementioned bipolar conduction, i.e., the activation of minority carriers across the narrow band gap. On the other hand, isovalent $Ru_2TiSi$, a novel fH compound recently studied by Fujimoto *et al.* [29], displays a much larger Seebeck coefficient and a broad maximum, vastly surpassing all other known fH compounds over the entire temperature range. This has motivated us to experimentally and theoretically study electronic transport in $Ru_2TiSi$ in detail and assess its potential thermoelectric performance at optimized doping.

## II. EXPERIMENTAL METHODS AND MODELING

Polycrystalline $Ru_2TiSi_{1-x}Al_x$ materials have been synthesized by melting raw elements with high-purity (99.99% Ru, 99.95% Ti, 99.9999% Si, and 99.999% Al) using a high-frequency induction-heating furnace. Even though powder x-ray diffraction investigations displayed a single Heusler phase directly after the melting procedure, the samples have been further annealed at 1273 K for 2 days in vacuum ($10^{-5}$ mbar) to optimize homogeneity. The samples have then been cut using a high-speed cutting device (Accutom by Struers) equipped with a diamond cutting wheel. The electrical resistivity and Seebeck coefficient at high temperatures were measured in the temperature range 300–860 K in an inert He atmosphere, using a commercially available setup (ZEM3 by ULVAC-RIKO). To analyze the temperature- and carrier-concentration-dependent Seebeck coefficient, we employed a least-squares-fit model based on Boltzmann-transport theory and the parabolic band approximation, as implemented in the SeeBand software [30]. Within this framework, thermoelectric transport is modeled by numerically solving the respective Fermi-transport integrals and summing up the contributions of the individual bands, assuming parallel conduction through two transport channels, i.e., one valence band and one conduction band.

## III. RESULTS AND DISCUSSION

### A. $Ru_2TiSi$ versus $Fe_2VAl$

In order to understand the thermoelectric properties and enhanced performance of $Ru_2TiSi$, a natural question would be what distinguishes it from the archetypal thermoelectric fH compound $Fe_2VAl$. In Fig. 2(a), we show the electronic density of states (DOS) of $Ru_2TiSi$ and $Fe_2VAl$ [31]. Both compounds display a deep well-pronounced pseudogap at the Fermi energy $E_F$, although the gap is significantly wider for $Ru_2TiSi$. Note that this pseudogap arises from the hybridization between the transition metal and the main-group-II or -IV elements, along with the absence of significant *d-d* hybridization [32]—a mechanism different from the ones frequently discussed in the context of high-temperature cuprate superconductors. Additionally, similar to $Fe_2VAl$, the DOS of $Ru_2TiSi$ is characterized by sharp peaks (owing to the rather localized Ru-4*d* states) rising next to both edges of the pseudogap, which results in a large differential DOS. Additionally, there are many more dispersive states (with a small DOS) dangling into the gap region, hereafter referred to as *pseudogap states*. It has been shown in previous studies that in $Fe_2VAl$, electronic transport is almost exclusively governed by these pseudogap states. In Fig. 2(b), we show the DOS around $E_F$ and a close-up of these pseudogap states. One can immediately note that the pseudogap states are much broader and the DOS much smaller for $Ru_2TiSi$ than for $Fe_2VAl$, especially at $E < E_F$. This implies much lighter more mobile charge carriers when $E_F$ is placed in the vicinity of these states. Moreover, the lower-DOS effective mass $m^*_{\mathrm{DOS}}$ suggests a much more efficient doping scenario for $Ru_2TiSi$. We illustrate this by drawing and comparing the Fermi level of hole-doped $Fe_2VAl$ (gray dashed line) and $Ru_2TiSi$ (purple dashed line) for a hole doping concentration of 0.05 holes per formula unit, assuming rigid-band doping. This corresponds approximately to the concentration for which *p*-type $Fe_2VAl$ displays its optimal thermoelectric performance. It can be seen that while for $Fe_2VAl$, this would place $E_F$ about 0.2 eV below the valence-band edge, $E_F$ is shifted by

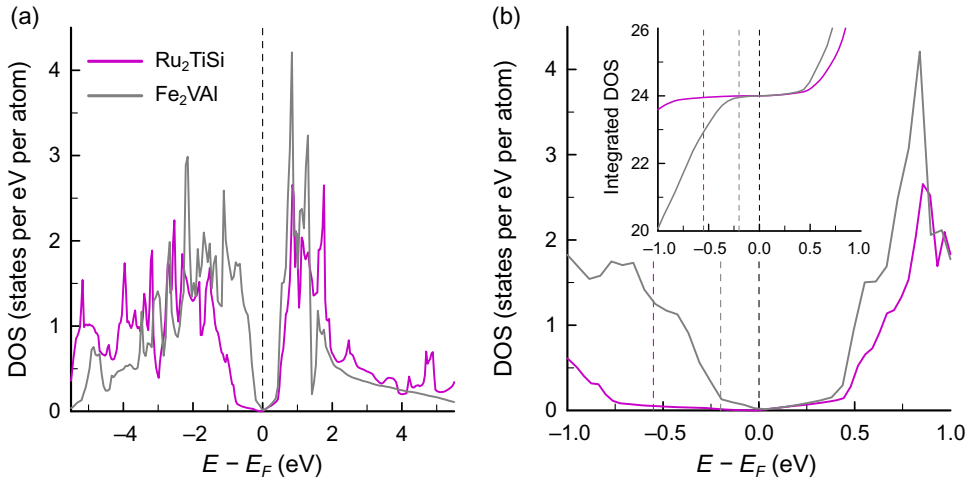


FIG. 2. The electronic density of states (DOS) of the fH compounds $Ru_2TiSi$ and $Fe_2VAl$. (a) A deep pseudogap with an almost negligibly small DOS at the Fermi level is present in both compounds, which is framed by sharp features in the DOS, originating from rather localized Fe-3*d* and Ru-4*d* states. (b) A close-up around the Fermi energy emphasizes that the pseudogap is much broader in $Ru_2TiSi$. Additionally, it can be seen that the dispersive pseudogap states, reaching into the gap region (small DOS), especially the valence-band states, have a much larger bandwidth and are therefore even more dispersive for $Ru_2TiSi$ compared to $Fe_2VAl$. The black dashed line indicates the Fermi energy $E_F$ and the gray and purple dashed lines show $E_F$ for a rigid-band doping scenario with 0.05 holes per formula unit. The inset shows the integrated DOS of both compounds.

almost 0.6 eV into the valence band for $Ru_2TiSi$. Hence, a significantly smaller number of holes has to be doped to reach optimal performance [compare also with the integrated DOS in the inset of Fig. 2(b)]. Interestingly, the difference in $m^*_{\mathrm{DOS}}$ appears less sizeable for the conduction band at $E > E_F$.

In Figs. 3(a) and 3(b), we display the temperature-dependent and doping-concentration-dependent Seebeck coefficient ($S(T)$ and $S(p,n)$), respectively. In Fig. 3(a), we model experimental $S(T)$ data of $Fe_2VAl$ and $Ru_2TiSi$ available in the literature [26,29], by employing a two-parabolic-band (2PB) least-squares-fit model as implemented in the SeeBand software package [30]. To fit the data, three independent fit parameters are adjusted: (i) the position of the Fermi level; (ii) the band gap or overlap $E_g$; and (iii) a weighting parameter $\epsilon_m = (N_{\mathrm{VB}} m^*_{\mathrm{CB}})/(N_{\mathrm{CB}} m^*_{\mathrm{VB}})$, which includes the degeneracies $N_i$ and effective masses $m_i$ of the two bands ($i = \{\mathrm{VB}, \mathrm{CB}\}$). $E_F$ determines the slope of $S(T)$ at low temperatures, $E_g$ the maximum Seebeck coefficient $S_{\max}$ as well as the temperature of the maximum $T_{\max}$, and $\epsilon$ dictates the sharpness of the maximum, i.e., the tail of $S(T)$ in the bipolar regime at temperatures above $T_{\max}$. Details regarding the modeling framework, which we have previously applied successfully to a number of fH [19,46] and skutterudite thermoelectric materials [48], are described in Ref. [30]. As for $Fe_2VAl$, excellent agreement with the experimental data is also found for $Ru_2TiSi$. The somewhat similar slope of $S(T)$ at low temperatures for $Fe_2VAl$ and the extrapolated curve of the 2PB model for $Ru_2TiSi$ indicate a comparable position of $E_F$ with respect to the valence-band edge. The most notable difference, however, is that $S_{\max}$ is shifted toward much higher temperatures in $Ru_2TiSi$ and reaches a very broad maximum of almost 200 $\mu\mathrm{V\,K^{-1}}$, as opposed to only 70–80 $\mu\mathrm{V\,K^{-1}}$ in $Fe_2VAl$.

In Fig. 3(b), we show the room-temperature Seebeck coefficient as a function of the hole ($p$) and the electron ($n$) doping concentration, calculated from the VEC via $p,n = 16\,n_{\mathrm{v}}/a^3$, where $a^3$ denotes the cubic-unit-cell volume of $Ru_2TiSi$ or $Fe_2VAl$ and 16 $n_{\mathrm{v}}$ represents the number of valence electrons in the unit cell. Each point refers to a different sample with a different VEC, which has been varied through aliovalent-element substitution. The data points have been taken from numerous doping studies in the literature and $p$-type $Ru_2TiSi_{1-x}Al_x$ compounds have been synthesized and investigated in the course of this work. The solid lines are theoretical calculations employing a 2PB model. Anand *et al.* have previously shown that the $S(p,n)$ dependence of $Fe_2VAl$ can be adequately described employing a 2PB model, assuming a small positive band gap of $E_g \approx 0.02$ eV and valence- and conduction-band effective masses of $m^*_{\mathrm{VB}} \approx 4.7\,m_e$ and $m^*_{\mathrm{CB}} \approx 12.8\,m_e$, respectively [22].

Contrary to $Fe_2VAl$, we find from our temperature- and doping-dependent analysis of the Seebeck coefficient of $Ru_2TiSi$ a much larger band gap of $E_g \approx 0.22$–$0.24$ eV and much lighter effective masses $m^*_{\mathrm{VB}} \approx 1.0\,m_e$ and $m^*_{\mathrm{CB}} \approx 3.3\,m_e$. The effect of the latter is directly visible in the much more rapid decrease of $S$ as $p$ and $n$ increase and is consistent with the smaller DOS and broader bandwidth of the pseudogap states of $Ru_2TiSi$ shown in Fig. 2(b). For $p$-type $Ru_2TiSi_{1-x}Al_x$, for instance, $S(300\ \mathrm{K})$ decreases

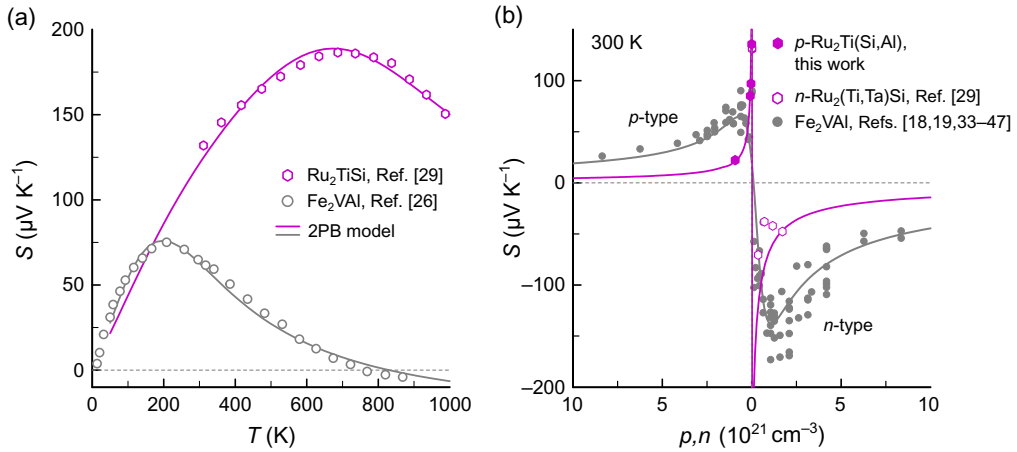


FIG. 3. Modeling of the thermoelectric transport in $Fe_2VAl$ and $Ru_2TiSi$ fHs. (a) A comparison of the temperature-dependent Seebeck coefficients of $Fe_2VAl$ and $Ru_2TiSi$. The experimental data have been taken from Refs. [26] and [29], respectively. The solid lines are least-squares fits employing a two-parabolic-band model, which captures the temperature-dependent $S(T)$ of both compounds in the entire temperature range excellently. (b) The doping-concentration-dependent Seebeck coefficient of $p$- and $n$-doped $Fe_2VAl$ and $Ru_2TiSi$ at room temperature. The Seebeck coefficient decreases much more rapidly as a function of the carrier concentration for the latter, indicating that doping is far more efficient in $Ru_2TiSi$ compared to $Fe_2VAl$, owing to the much lighter and more dispersive bands; $p$-type $Ru_2TiSi_{1-x}Al_x$-based compounds (filled symbols) have been synthesized and investigated in this work. The unfilled purple symbols have been taken from Ref. [29] and the filled gray symbols have been taken from various literature studies [18,19,33–47].

from 130 μV $K^{-1}$ in pristine $Ru_2TiSi$ down to only 22 μV $K^{-1}$ for $x = 0.05$. In this sense, the valence-band electronic structure of $Ru_2TiSi$ appears much more similar to those of chalcogenide semiconductors such as $Bi_2Te_3$ and PbTe, where the underlying DOS is composed of $s$- and $p$-like states with a larger bandwidth (low $m^*_{DOS}$), rather than hH and fH compounds, where usually a much larger doping concentration is required due to the more localized nature of the $d$ orbitals building up the DOS (high $m^*_{DOS}$). At this point, we also note that, interestingly, $S(n)$ first decreases and then increases with $n$ for $n$-type $Ru_2Ti_{1-x}Ta_xSi$ reported in Ref. [29], instead of monotonically decreasing. While this might be within the margin of experimental uncertainty, it could also be an indication of the contribution of a second conduction band as $E_F$ is shifted further toward higher energies with increasing Ta substitution. Indeed, this would be consistent from a purely rigid-band-like shift of $E_F$, considering the DOS presented in Fig. 2(b), which changes its slope around $0.4 - 0.5$ eV above $E_F$.

### B. Detailed analysis of $p$- and $n$-doped $Ru_2TiSi$

Next, we present a detailed analysis of the temperature-dependent transport properties of $n$-type $Ru_2Ti_{1-x}Ta_xSi$ from Ref. [29] and $p$-type $Ru_2TiSi_{1-x}Al_x$ from this work. In Fig. 4(a), we display the $S(T)$ data of the former, collected by Fujimoto *et al.* in the temperature range 300–1000 K. Least-squares fits using the 2PB model are again able to reproduce all the measured curves reasonably well. Particularly striking is the distinct maximum in $S(T)$ at 700 K, followed by a sign reversal of $S(T)$ at around 900 K for $Ru_2Ti_{0.97}Ta_{0.03}Si$. This is a direct signature of the strong electron-hole asymmetry and the much higher mobility of holes compared to the conduction-band electrons. This is directly reflected in the weighting parameter $\epsilon_m$ derived from our fit. A large $\epsilon_m$ implies that either a much larger degenerate set of hole pockets (compared to the electron pockets) contributes to the transport properties and/or that conduction-band electrons are much heavier compared to the hole-type carriers. An extraordinarily large value of $\epsilon_m \approx 60$ is found for $Ru_2Ti_{0.97}Ta_{0.03}Si$ (and even larger values are found for higher Ta concentrations; see Appendix C), which is especially remarkable considering that $N_{VB} = N_{CB} = 3$ is derived from band-structure calculations provided in the Materials Project open web database [49]. We attribute this extreme electron-hole asymmetry to the very dispersive valence-band and the much more localized and heavy conduction-band states, approximately 0.5 eV above $E_F$ [see Fig. 2(b)]. These states likely become important at elevated temperatures and higher doping concentrations, which explains why a much smaller band asymmetry $\epsilon_m \approx 3.3$ is derived from the analysis of the doping-dependent Seebeck coefficient of $Ru_2TiSi$-based compounds at 300 K, shown in Fig. 3(b). Nonetheless, this band asymmetry is likely critical for the thermoelectric performance of $Ru_2TiSi$, which peaks at much higher temperatures $T > 300$ K.

The notion of much lighter holes compared to the conduction electrons is also confirmed when examining

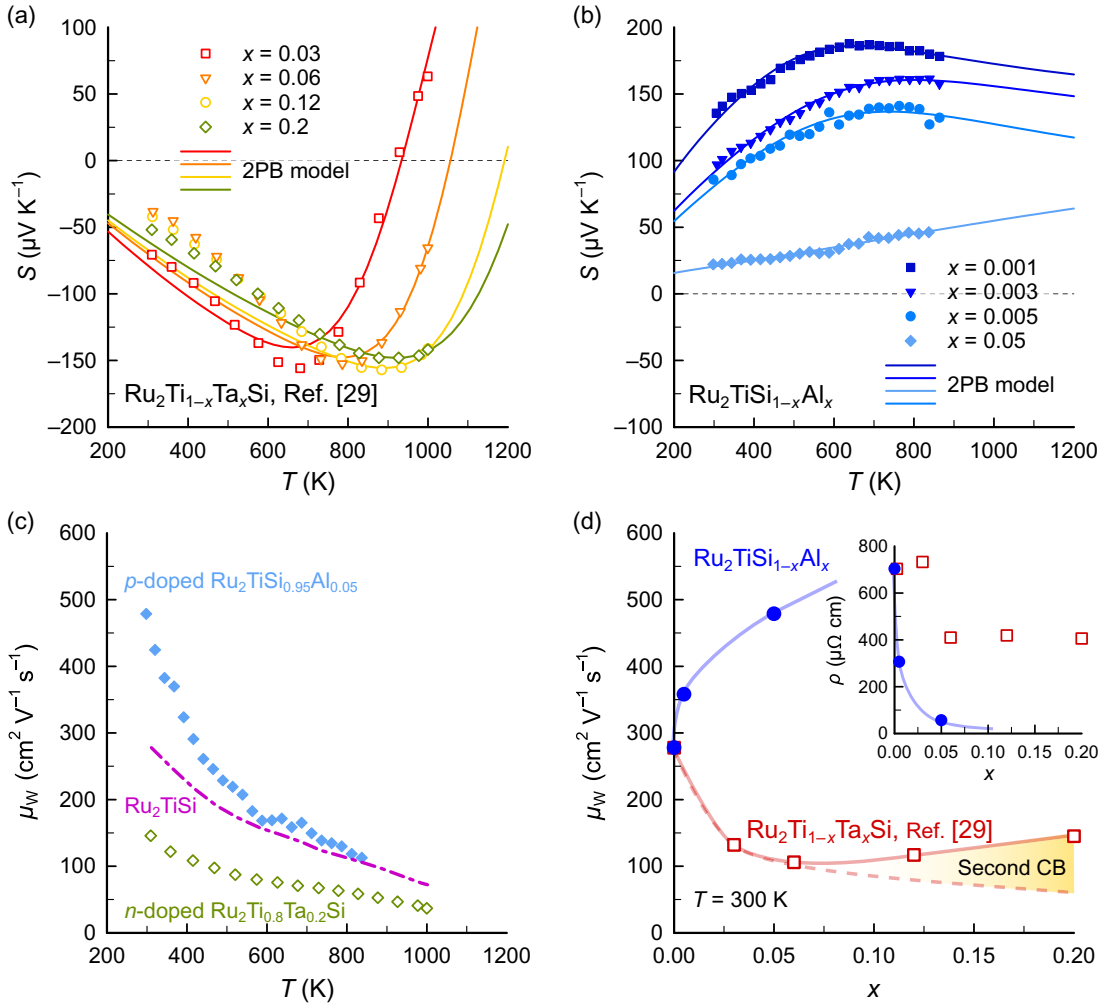


FIG. 4. The electron-hole band asymmetry in $Ru_2TiSi$. The temperature-dependent Seebeck coefficient $S(T)$ of (a) $n$-type $Ru_2Ti_{1-x}Ta_xSi$ from Ref. [29] and (b) $p$-type $Ru_2TiSi_{1-x}Al_x$ from this work. The solid lines are least-squares fits employing a two-parabolic-band model. Notably, the maximum in $|S(T)|$ is much sharper for $n$-type $Ru_2Ti_{1-x}Ta_xSi$ and even a sign reversal of the Seebeck coefficient takes place, once minority carriers from the valence band are activated. This implies that holes are much more mobile than carriers occupying the conduction-band states in $Ru_2TiSi$. For $p$-type $Ru_2TiSi_{1-x}Al_x$, the maximum in $|S(T)|$ is much broader and doping is much more efficient, i.e., a substitution of only a few at.% Al for Si results in a strong decrease of $S(T)$ as $E_F$ moves rapidly away from the band edge. (c) The weighted-mobility comparison of heavily $n$-doped $Ru_2Ti_{0.8}Ta_{0.2}Si$, pristine $Ru_2TiSi$, and heavily $p$-doped $Ru_2TiSi_{0.95}Al_{0.05}$. (d) The composition-dependent weighted mobility evaluated at 300 K. The solid and dashed lines are a guide to the eye, with the yellow area corresponding to an expected gain in $\mu_W$ arising from the contribution of a second conduction band. Most importantly, $\mu_W$ is much greater for $p$-type $Ru_2TiSi$, confirming its superiority over $n$-type $Ru_2TiSi$. The inset shows the corresponding composition-dependent resistivity.

the temperature-dependent Seebeck coefficient of $p$-type $Ru_2TiSi_{1-x}Al_x$ in Fig. 4(b). Both the experimental data collected in this study and the 2PB model extrapolating toward higher temperatures show a much broader maximum of $S(T)$, almost saturating at high temperatures. This demonstrates that the weighted contribution of the minority carriers, activated at high temperatures, is small. In Figs. 4(c) and 4(d), we display the temperature- and composition-dependent weighted mobility $\mu_W$. The weighted mobility, $\mu_W \approx \mu_D \left(m^*_{DOS}/m_e\right)^{3/2}$, is a temperature-dependent material property, which, unlike the drift mobility $\mu_D$ and the Hall mobility $\mu_H$, is independent of the carrier concentration—at least within the parabolic band approximation. From a thermoelectric perspective, $\mu_W$ represents a unique relationship between $S$ and $\sigma$ and determines the maximum figure of merit $z$ that can be achieved at optimized doping. We have calculated $\mu_W$ via the scheme presented in Ref. [50]. Despite the limitations of such an analysis owing to (i) bipolar transport and (ii) the rather complex band structure, particularly concerning the conduction-band states, it is nonetheless obvious that $\mu_W$ is several times larger for $p$-doped

$Ru_2TiSi$, as opposed to the *n*-doped compounds reported previously [29]. The increase of $\mu_W$ with increasing Al concentration $x$ in $Ru_2TiSi_{1-x}Al_x$ is anomalous and hints at either (i) contributions from additional valence bands as $E_F$ is lowered deeper into the valence-band states, (ii) deviation of parabolicity of the contributing band valleys, or (iii) a change in the dominant carrier-scattering mechanism. For instance, it is well known that in intrinsic semiconductors, such as pristine $Ru_2TiSi$, tiny amounts of ionized impurities can limit carrier transport, while with an increase in the carrier concentration, these impurities become screened, enhancing the mobility. In the highly doped regime, $\mu_W$ is most likely primarily limited by charge carriers scattering off phonons and random potential fluctuations caused by the alloy disorder at the Si site.

### C. Assessing optimal thermoelectric performance

To evaluate the optimal performance of *p*- and *n*-type $Ru_2TiSi$, we have modeled the composition-dependent power factor $PF = S^2\sigma$—the product of the Seebeck coefficient squared, $S^2$, and the electrical conductivity $\sigma$—and the thermal conductivity. The maximum $zT$ has been estimated based on these theoretical results. In Fig. 5(a), we show the carrier doping-dependent $PF$ at 300 K and 700 K. Despite some limitations, our 2PB model traces the trend of the experimental data fairly well and correctly reproduces the enhanced performance of the *p*-type compounds. The electronic part of the thermal conductivity has been calculated via the Wiedemann-Franz law, following the same procedure as described in Ref. [22]. The lattice thermal conductivity $\kappa_L$, shown in Fig. 5(b), can be described by a simple alloy-scattering model [22], which considers two primary scattering contributions, namely, (i) Umklapp phonon-phonon scattering and (ii) scattering of high-frequency phonons with point defects introduced by the random substitution of other atoms in the compound. The latter depends on mass and volume fluctuations and is especially significant when substituting heavy 5*d* elements, e.g., Ta instead of Ti. Following this argument, one may assume that other 5*d* elements with similar atomic mass and size, such as Hf, would have a similar effect and composition dependence of $\kappa_L$, which is indeed what is observed in $Fe_2VAl$ fH compounds as well [51]. According to the Materials Project database, $Ru_2HfSi$ is also a theoretically predicted stable Heusler compound, as is $Ru_2ZrSi$, both with a very similar electronic structure to $Ru_2TiSi$. This suggests that alloying of $Ru_2TiSi$ with $Ru_2ZrSi$ and $Ru_2HfSi$ could be possible, consequently leading to reduced $\kappa_L$ and hence increased $zT$. Since the

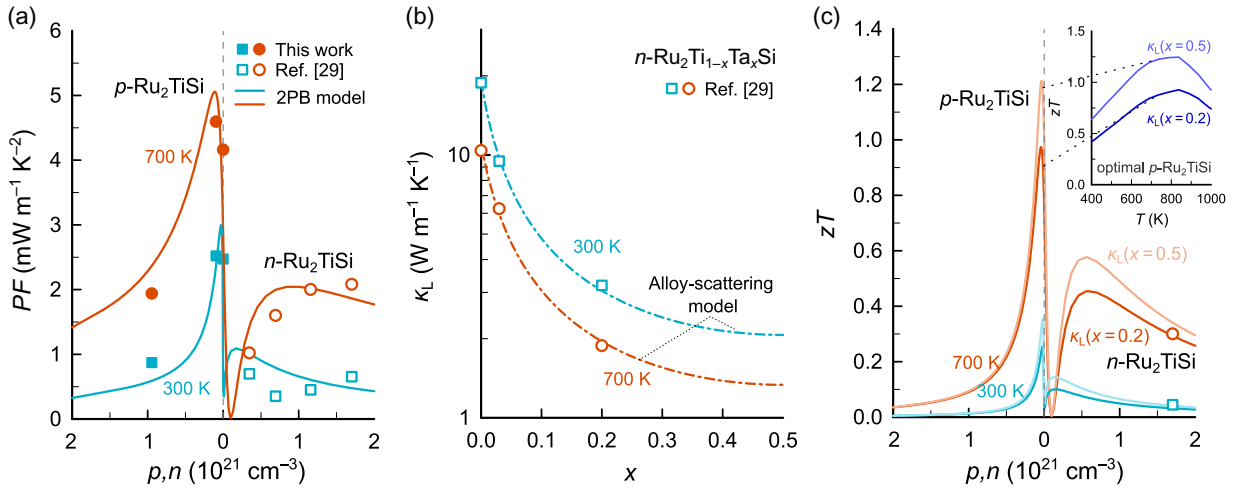


FIG. 5. Modeling and estimation of the thermoelectric performance in $Ru_2TiSi$-based fH compounds. (a) The doping-concentration-dependent power factor $PF$ of $Ru_2TiSi$ at 300 K and 700 K. The open and filled symbols are experimental data from this work and from Ref. [29], respectively. The solid lines are theoretical calculations using a two-parabolic-band model. A more than 2 times larger $PF$ is predicted (and experimentally achieved) for *p*-type $Ru_2TiSi$ due to the superior quality of the valence-band structure. At a fixed geometry and for a given temperature difference, the power factor determines the power output that can be generated within a thermoelectric device. (b) The composition-dependent trend of the lattice thermal conductivity for $Ru_2Ti_{1-x}Ta_xSi$ from Ref. [29]. The dashed-dotted lines have been calculated employing a simple alloy-scattering model [22]. The large mass and volume fluctuations imposed by the substitution with heavy 5*d* elements effectively scatter high-frequency heat-carrying phonons. (c) The doping-concentration-dependent $zT$ of $Ru_2TiSi$ at 300 K and 700 K. The power factor $PF$ and the electronic contribution to the thermal conductivity have been calculated employing a two-parabolic-band model. The lattice thermal conductivity has been estimated from (b) under the reasonable assumption that the substitution with other 5*d* elements, such as Hf/Ti, results in a similar suppression of $\kappa_L$. Hf substitution does not change the total number of valence electrons and, therefore, it remains near the predicted maximum $zT$, exceeding $zT = 1$ at 700 K, especially in the case in which a full solid solution between $Ru_2TiSi$ and $Ru_2HfSi$ is possible. The inset shows the temperature-dependent $zT$ at optimal doping.

valence-band states of fH compounds, such as $Fe_2VAl$ and $Ru_2TiSi$, are almost exclusively governed by the $X$ atoms, introducing disorder at the $Y$ site hardly affects the electronic transport properties and retains high values of the weighted mobility [22]. On the other hand, the pseudogap states of the conduction band have a $Y$-$e_g$ orbital character, which results in a strong trade-off between $\kappa_L$ and $\mu_W$. Thus, substituting heavy $5d$ elements at the Ti site would be especially promising for $p$-type $Ru_2TiSi$, where $E_F$ is located in the Ru-$t_{2g}$ valence bands.

In Fig. 5(c), we show the theoretical prediction of the doping-dependent $zT$ for an alloy of $Ru_2TiSi$ and $Ru_2HfSi$ from our 2PB model, assuming similar electronic transport. The darker colors refer to a 20% Ti-Hf substitution, while the lighter colors refer to a 50% alloy, minimizing the lattice thermal conductivity of the compound. For the $Ru_2Ti_{0.5}Hf_{0.5}Si$ alloy, our calculations predict a high maximum $zT = 1 - 1.2$ at 700 K for optimal doping, which motivates experimental exploration of this virginal material platform and showcases that not only hH but also fH compounds bear the potential for competitive thermoelectric performance.

## IV. CONCLUSIONS

To summarize, we have investigated thermoelectric transport of $Ru_2TiSi$-based fH compounds and compared their transport properties to those of $Fe_2VAl$. A two-parabolic-band model accurately captures the temperature- and doping-dependent thermoelectric transport properties of $Ru_2TiSi$. The resulting effective band structure underlies that the valence-band electronic structure displays much greater potential for realizing high thermoelectric performance compared to $p$-type $Fe_2VAl$. Moreover, we predict that $p$-type $Ru_2TiSi$ would outperform $n$-type compounds, studied previously, by a factor of 2–3, potentially realizing $zT > 1$ at 700 K upon appropriate reduction of the lattice thermal conductivity, e.g., by isovalent substitution with Zr or Hf at the Ti site. Our work encourages further investigation of the vast phase space of fH next to hH compounds as thermoelectric materials.

## ACKNOWLEDGMENTS

F.G., M.P., E.B., and T.M. were financially supported by the Japan Science and Technology Agency (JST) program MIRAI, JPMJMI19A1. A.P. acknowledges support from OeAD WTZ (Projects CZ 08/2023 and HR 05/2024).

## DATA AVAILABILITY

The experimental data are available at TU Wien's research data respository [52].

## APPENDIX A: STRUCTURAL PROPERTIES

The structural properties and phase purity of the $p$-type $Ru_2TiSi_{1-x}Al_x$ Heusler compounds synthesized and investigated in this work have been studied using x-ray powder diffraction (XRPD), making use of a commercially available diffractometer (AERIS by PANalytical). Cu $K\alpha$ radiation has been used and measurements have been conducted in a Bragg-Brentano geometry. An exemplary XRPD pattern for the sample with the largest amount of Al substitution, i.e., $Ru_2TiSi_{0.95}Al_{0.05}$, is shown in Fig. 6 together with Rietveld refinements, which have been performed using the program PowderCell. The powder pattern displays a single fH ($L2_1$ structure) phase with a lattice parameter $a \approx 0.5967$ nm derived from the Rietveld refinement. The room-temperature lattice parameter is only about 0.14% larger than that of pristine $Ru_2TiSi$ [29], which aligns with expectations, since the atomic radii of silicon ($r_{Si} \approx 111$ pm) and aluminum ($r_{Al} \approx 125$ pm) are quite similar.

## APPENDIX B: ELECTRICAL RESISTIVITY

In Fig. 7, we summarize the temperature-dependent electrical resistivity $\rho(T)$ of the $Ru_2TiSi$ system. First, $\rho(T)$ of pristine $Ru_2TiSi$ from Ref. [29] is compared with $\rho(T)$ of pristine $Fe_2VAl$ from Ref. [26] in Fig. 7(a). Despite the larger band gap, evident from the larger Seebeck coefficient of $Ru_2TiSi$, the resistivity at low temperatures is actually lower compared to $Fe_2VAl$. We attribute this to the fact that $Ru_2TiSi$ is intrinsically doped, with $E_F$ located about 0.06 eV below the valence band edge. Thus, at low temperatures $\rho(T)$ should show metalliclike behavior, as is indeed observed. Fujimoto *et al.* have reported a carrier mobility of around 100 $cm^2\,V^{-1}\,s^{-1}$ for pristine $Ru_2TiSi$ [29], about an order of magnitude larger than

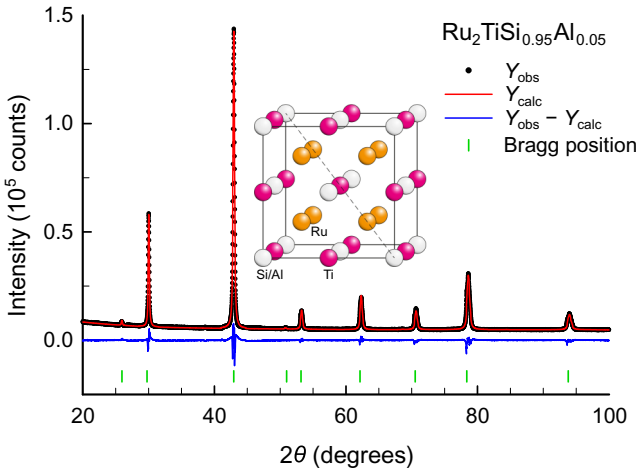


FIG. 6. The x-ray powder diffraction pattern of phase-pure $p$-type $Ru_2TiSi_{0.95}Al_{0.05}$ alongside Rietveld refinement. The inset shows the fH crystal structure.

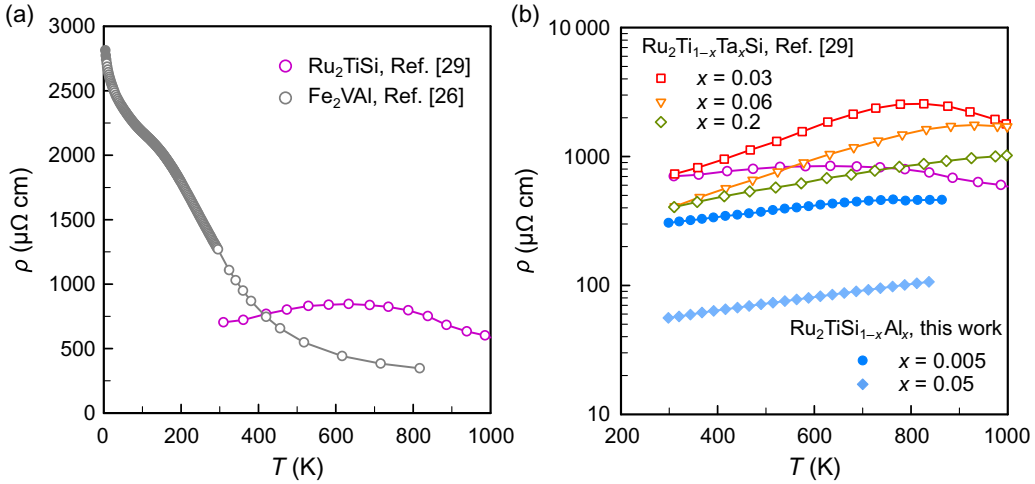


FIG. 7. The temperature-dependent electrical resistivity of $Ru_2TiSi$ Heusler compounds. (a) The temperature-dependent electrical resistivity of pristine $Ru_2TiSi$ [29] compared to that of pristine $Fe_2VAl$ [26]. Although $Ru_2TiSi$ has a larger band gap, the electrical resistivity, especially at low temperatures, is lower than that of $Fe_2VAl$, highlighting that $E_F$ is intrinsically doped in the valence band, which, due to its lower effective mass, enables a higher carrier mobility and lower resistivity for $Ru_2TiSi$. (b) The temperature-dependent resistivity for different $n$- and $p$-doped $Ru_2TiSi$ samples from Ref. [29] and this work, respectively. It is evident that for $p$-type $Ru_2TiSi_{1-x}Al_x$, $\rho(T)$ decreases much more rapidly as a function of the doping concentration.

that of $Fe_2VAl$. The carrier mobility in undoped $Fe_2VAl$ is not only smaller due to less dispersive bands at $E_F$ but also hampered by pivotal carrier scattering off localized in-gap impurity states arising from intrinsic Fe-V and Fe-Al exchange antisite defects [53]. It is possible that the formation of such antisite defects, involving the Ru sublattice, is suppressed in $Ru_2TiSi$ due to the larger atomic size mismatch between Ru and Ti-Si, as opposed to Fe versus V-Al.

In Fig. 7(b), we show $\rho(T)$ for various $n$- and $p$-doped $Ru_2TiSi$-based fHs from Ref. [29] and this work, respectively. It is evident that for $p$-type compounds, $\rho(T)$ decreases extremely quickly, again reflecting the dispersive nature of the valence-band electronic structure. For $Ru_2TiSi_{1-x}Al_x$, an Al substitution of only $x = 0.05$ yields a very strong decrease of the room-temperature resistivity down to only 56 μΩ cm, which is comparable to that of ordinary metals.

## APPENDIX C: FIT PARAMETERS

In Table I, we list the obtained fit parameters from our analysis of the temperature-dependent Seebeck coefficient of $n$-type $Ru_2Ti_{1-x}Ta_xSi$ from Ref. [29] and $p$-type $Ru_2TiSi_{1-x}Al_x$ from this work. There are three independent fit parameters that can be extracted to develop an effective band-structure model. The first parameter, $\epsilon_m$, serves as a weighting parameter, which represents the weighted contribution between the two bands. The larger $\epsilon_m$ is, the smaller is the weighted contribution of the conduction-band carriers. Since $m_{VB} \approx 1\, m_e$ could be derived from the carrier-concentration dependence of $S$ and because $N_{VB} = N_{CB} \approx 3$, $\epsilon_m$ can be considered the effective mass of the conduction-band electrons $\epsilon_m \sim m_{CB}$. Taking a look at the values in Table I, it is clear that $m_{CB}$ increases dramatically with Ta substitution and sort of saturates at very large values of several hundred times the free electron mass [left axis in Fig. 8(a)]. This aligns with the notion of a second, much heavier, conduction band, further above $E_F$, which is also observed in $Fe_2VAl$ and similar Heusler compounds and the origin of which has been extensively discussed by Bilc *et al.* [54]. Similarly, the band gap derived from our 2PB model

TABLE I. The fit parameters obtained from modeling the temperature-dependent Seebeck coefficient of $Ru_2Ti_{1-x}Ta_xSi$ and $Ru_2TiSi_{1-x}Al_x$. The values of the Fermi energy are given with respect to the valence-band/conduction-band edge for $p$- and $n$-type samples respectively.

| Sample | $x$ | $\epsilon_m$ | $E_g$ (eV) | $E_F$ (eV) |
|---|---|---|---|---|
| $n$-type $Ru_2Ti_{1-x}Ta_xSi$ | 0 | 1.2 | 0.24 | −0.06 |
| | 0.03 | 62 | 0.42 | 0.09 |
| | 0.06 | 392 | 0.67 | 0.11 |
| | 0.12 | 385 | 0.78 | 0.11 |
| | 0.20 | 239 | 0.74 | 0.12 |
| $p$-type $Ru_2TiSi_{1-x}Al_x$ | 0 | 1.2 | 0.24 | −0.06 |
| | 0.001 | 3.4 | 0.18 | −0.05 |
| | 0.003 | 2.1 | 0.16 | −0.08 |
| | 0.005 | 1.5 | 0.11 | −0.09 |
| | 0.05 | ... | ... | −0.26 |

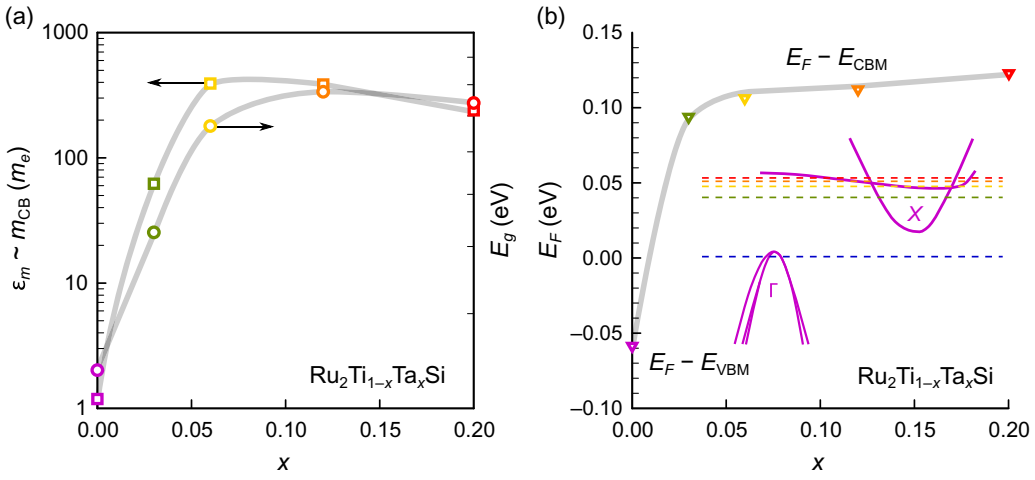


FIG. 8. The evolution of the electronic structure in $n$-doped $Ru_2Ti_{1-x}Ta_xSi$, extracted from fits of the temperature-dependent Seebeck coefficient. (a) The concentration-dependent weighting parameter $\epsilon_m$ (left axis) and band gap $E_g$ (right axis) of $n$-type $Ru_2Ti_{1-x}Ta_xSi$. The former corresponds to the effective mass of the conduction band, given that $m_{VB} \approx 1\, m_e$ and $N_{VB} = N_{CB}$. Both $\epsilon_m \sim m_{CB}$ and $E_g$ extracted from our 2PB fits increase with $x$ as $E_F$ is shifted further toward the flat band, located 0.75 eV above the top of the valence bands. (b) The doping level of $n$-type $Ru_2Ti_{1-x}Ta_xSi$. $E_F$ jumps abruptly from the valence toward the conduction band but saturates with increasing $x$ due to the high DOS of the flat-band states.

seemingly increases with $x$ and saturates at around 0.7–0.8 eV [right axis in Fig. 8(a)]. We interpret this as the position of the second conduction-band minimum with respect to the valence-band top. The Fermi level $E_F$, which is given with respect to the top of the valence band for $p$-type and with respect to the bottom of the conduction band for $n$-type samples, rapidly jumps from the top of the valence band and is shifted into the conduction-band states. As $x$ increases further, however, $E_F$ almost saturates and is seemingly pinned in the conduction band [see Fig. 8(b)], which is another indirect proof of the flat and heavy band and its associated high DOS that prevents efficient doping (shifts of $E_F$). A schematic of the effective band structure expected for $Ru_2TiSi$, the respective energy gaps, and the position of the Fermi level is presented in Fig. 8(b).

To summarize, there is conclusive evidence from various fit parameters obtained by modeling the temperature-dependent Seebeck coefficient that $Ru_2TiSi$ is a narrow-gap semiconductor with dispersive valence- and conduction-band states and significant electron-hole asymmetry arising from another conduction band hosting charge carriers that are orders of magnitude heavier. This becomes particularly important when $E_F$ is shifted deep into the conduction bands via $n$-type doping, or at high temperatures, where states further away from $E_F$ become excited.

[1] T. Graf, C. Felser, and S. S. Parkin, Simple rules for the understanding of Heusler compounds, Prog. Solid State Chem. **39**, 1 (2011).

[2] F. Casper, T. Graf, S. Chadov, B. Balke, and C. Felser, Half-Heusler compounds: Novel materials for energy and spintronic applications, Semicond. Sci. Technol. **27**, 063001 (2012).

[3] K. Manna, Y. Sun, L. Muechler, J. Kübler, and C. Felser, Heusler, Weyl and Berry, Nat. Rev. Mater. **3**, 244 (2018).

[4] I. Galanakis, P. Dederichs, and N. Papanikolaou, Slater-Pauling behavior and origin of the half-metallicity of the full-Heusler alloys, Phys. Rev. B **66**, 174429 (2002).

[5] I. Galanakis, P. Mavropoulos, and P. H. Dederichs, Electronic structure and Slater-Pauling behaviour in half-metallic Heusler alloys calculated from first principles, J. Phys. D: Appl. Phys. **39**, 765 (2006).

[6] S. Skaftouros, K. Özdoğan, E. Şaşıoğlu, and I. Galanakis, Generalized Slater-Pauling rule for the inverse Heusler compounds, Phys. Rev. B—Condens. Matter Mater. Phys. **87**, 024420 (2013).

[7] M. Parzer, F. Garmroudi, A. Riss, S. Khmelevskyi, T. Mori, and E. Bauer, High solubility of Al and enhanced thermoelectric performance due to resonant states in $Fe_2VAl_x$, Appl. Phys. Lett. **120**, 071901 (2022).

[8] M. Parzer, F. Garmroudi, A. Riss, M. Reticcioli, R. Podloucky, M. Stöger-Pollach, E. Constable, A. Pustogow, T. Mori, and E. Bauer, Semiconducting Heusler compounds beyond the Slater-Pauling rule, PRX Energy **3**, 033006 (2024).

[9] W. G. Zeier, J. Schmitt, G. Hautier, U. Aydemir, Z. M. Gibbs, C. Felser, and G. J. Snyder, Engineering half-Heusler thermoelectric materials using Zintl chemistry, Nat. Rev. Mater. **1**, 1 (2016).

[10] S. Anand, M. Wood, Y. Xia, C. Wolverton, and G. J. Snyder, Double half-Heuslers, Joule **3**, 1226 (2019).

[11] L. Wang, Z. Dong, S. Tan, J. Zhang, W. Zhang, and J. Luo, Discovery of a Slater-Pauling semiconductor $ZrRu_{1.5}Sb$ with promising thermoelectric properties, Adv. Funct. Mater. **32**, 2200438 (2022).

[12] J. Zhang, Z. Dong, S. Tan, Y. Li, J. Zhang, W. Zhang, and J. Luo, Designing vacancy-filled Heusler thermoelectric semiconductors by the Slater-Pauling rule, Mater. Today Energy **27**, 101035 (2022).

[13] G. J. Snyder and E. S. Toberer, Complex thermoelectric materials, Nat. Mater. **7**, 105 (2008).

[14] T. Zhu, C. Fu, H. Xie, Y. Liu, and X. Zhao, High efficiency half-Heusler thermoelectric materials for energy harvesting, Adv. Energy Mater. **5**, 1500588 (2015).

[15] G. Rogl and P. F. Rogl, Development of thermoelectric half-Heusler alloys over the past 25 years, Crystals **13**, 1152 (2023).

[16] W. Li, S. Ghosh, N. Liu, and B. Poudel, Half-Heusler thermoelectrics: Advances from materials fundamental to device engineering, Joule **0**, 0 (2024).

[17] V. Pecunia, S. R. P. Silva, J. D. Phillips, E. Artegiani, A. Romeo, H. Shim, J. Park, J. H. Kim, J. S. Yun, and G. C. Welch *et al.*, Roadmap on energy harvesting materials, J. Phys.: Mater. **6**, 042501 (2023).

[18] Y. Nishino, S. Deguchi, and U. Mizutani, Thermal and transport properties of the Heusler-type $Fe_2VAl_{1-x}Ge_x$ ($0 \leq x \leq 0.20$) alloys: Effect of doping on lattice thermal conductivity, electrical resistivity, and Seebeck coefficient, Phys. Rev. B—Condens. Matter Mater. Phys. **74**, 115115 (2006).

[19] F. Garmroudi, M. Parzer, A. Riss, S. Beyer, S. Khmelevskyi, T. Mori, M. Reticcioli, and E. Bauer, Large thermoelectric power factors by opening the band gap in semimetallic Heusler alloys, Mater. Today Phys. **27**, 100742 (2022).

[20] E. Alleno, A. Diack-Rasselio, M. Talla Noutack, and P. Jund, Optimization of the thermoelectric properties in self-substituted $Fe_2VAl$, Phys. Rev. Mater. **7**, 075403 (2023).

[21] H. Okamura, J. Kawahara, T. Nanba, S. Kimura, K. Soda, U. Mizutani, Y. Nishino, M. Kato, I. Shimoyama, and H. Miura *et al.*, Pseudogap formation in the intermetallic compounds $(Fe_{1-x}V_x)_3Al$, Phys. Rev. Lett. **84**, 3674 (2000).

[22] S. Anand, R. Gurunathan, T. Soldi, L. Borgsmiller, R. Orenstein, and G. J. Snyder, Thermoelectric transport of semiconductor full-Heusler $VFe_2Al$, J. Mater. Chem. C **8**, 10174 (2020).

[23] B. Hinterleitner, F. Garmroudi, N. Reumann, T. Mori, E. Bauer, and R. Podloucky, The electronic pseudo band gap states and electronic transport of the full-Heusler compound $Fe_2VAl$, J. Mater. Chem. C **9**, 2073 (2021).

[24] C.-S. Lue and Y.-K. Kuo, Thermoelectric properties of the semimetallic Heusler compounds $Fe_{2-x}V_{1+x}M$ ($M$ = Al, Ga), Phys. Rev. B **66**, 085121 (2002).

[25] C. Kuo, H. Lee, C.-M. Wei, Y. Lin, Y. Kuo, and C. Lue, $Ru_2NbGa$: A Heusler-type compound with semimetallic characteristics, Phys. Rev. B **94**, 205116 (2016).

[26] I. Knapp, B. Budinska, D. Milosavljevic, P. Heinrich, S. Khmelevskyi, R. Moser, R. Podloucky, P. Prenninger, and E. Bauer, Impurity band effects on transport and thermoelectric properties of $Fe_{2-x}Ni_xVAl$, Phys. Rev. B **96**, 045204 (2017).

[27] S. Mondal, C. Mazumdar, R. Ranganathan, E. Alleno, P. Sreeparvathy, V. Kanchana, and G. Vaitheeswaran, Ferromagnetically correlated clusters in semimetallic $Ru_2NbAl$ Heusler alloy and its thermoelectric properties, Phys. Rev. B **98**, 205130 (2018).

[28] S. Mondal, K. Ghosh, R. Ranganathan, E. Alleno, and C. Mazumdar, Thermoelectric properties of $Ru_2TiGe$ Heusler phase, J. Alloys Compd. **961**, 171050 (2023).

[29] T. Fujimoto, M. Mikami, H. Miyazaki, and Y. Nishino, Enhanced thermoelectric performance of $Ru_2TiSi$ Heusler compounds with Ta substitution, J. Alloys Compd. **969**, 172345 (2023).

[30] M. Parzer, A. Riss, F. Garmroudi, J. de Boor, T. Mori, and E. Bauer, SeeBand: A highly efficient, interactive tool for analyzing electronic transport data, arXiv:2409.06261.

[31] The computational DOS data have been taken from the Materials Project open web database [55].

[32] M. Weinert and R. Watson, Hybridization-induced band gaps in transition-metal aluminides, Phys. Rev. B **58**, 9732 (1998).

[33] E. J. Skoug, C. Zhou, Y. Pei, and D. T. Morelli, High thermoelectric power factor near room temperature in full-Heusler alloys, J. Electron. Mater. **38**, 1221 (2009).

[34] M. Vasundhara, V. Srinivas, and V. Rao, Electronic transport in Heusler-type $Fe_2VAl_{1-x}M_x$ alloys ($M$ = B, In, Si), Phys. Rev. B **77**, 224415 (2008).

[35] M. Vasundhara, V. Srinivas, and V. Rao, Low-temperature electrical transport in Heusler-type $Fe_2V(AlSi)$ alloys, J. Phys.: Condens. Matter **17**, 6025 (2005).

[36] C. S. Lue, C. Chen, J. Lin, Y. Yu, and Y. Kuo, Thermoelectric properties of quaternary Heusler alloys $Fe_2VAl_{1-x}Si_x$, Phys. Rev. B **75**, 064204 (2007).

[37] Y. Nishino *et al.*, in *2011 IOP Conf. Ser.: Mater. Sci. Eng.* (2011), Vol. 18, p. 142001.

[38] M. Mikami, K. Ozaki, H. Takazawa, A. Yamamoto, Y. Terazawa, and T. Takeuchi, Effect of Ti substitution on thermoelectric properties of W-doped Heusler $Fe_2VAl$ alloy, J. Electron. Mater. **42**, 1801 (2013).

[39] H. Nakayama, N. Ide, and Y. Nishino, Thermoelectric properties of $p$-type Heusler compounds $(Fe_{2-x}Co_x)(V_{1-y}Ti_y)Al$, Mater. Trans. **49**, 1858 (2008).

[40] Y. Terazawa, M. Mikami, T. Itoh, and T. Takeuchi, Effects of heavy element substitution on electronic structure and lattice thermal conductivity of $Fe_2VAl$ thermoelectric material, J. Electron. Mater. **41**, 1348 (2012).

[41] M. Mikami, Y. Kinemuchi, K. Ozaki, Y. Terazawa, and T. Takeuchi, Thermoelectric properties of tungsten-substituted Heusler $Fe_2VAl$ alloy, J. Appl. Phys. **111**, 093710 (2012).

[42] H. Kato, M. Kato, Y. Nishino, U. Mizutani, and S. Asano, Effect of silicon substitution on thermoelectric properties of Heusler-type $Fe_2VAl$ alloy, Nippon Kinzoku Gakkaishi (1952) **65**, 652 (2001).

[43] Y. Sandaiji, N. Ide, Y. Nishino, T. Ohwada, S. Harada, and K. Soda, Off-stoichiometric effects on thermoelectric properties of $Fe_2VAl$-based compounds, Funtai Oyobi Funmatsuyakin **57**, 207 (2010).

[44] W. Lu, W. Zhang, and L. Chen, Thermoelectric properties of $(Fe_{1-x}Co_x)_2VAl$ Heusler-type compounds, J. Alloys Compd. **484**, 812 (2009).

[45] B. Hinterleitner, P. Fuchs, J. Rehak, F. Garmroudi, M. Parzer, M. Waas, R. Svagera, S. Steiner, M. Kishimoto, and R. Moser *et al.*, Stoichiometric and off-stoichiometric full Heusler $Fe_2V_{1-x}W_xAl$ thermoelectric systems, Phys. Rev. B **102**, 075117 (2020).

[46] F. Garmroudi, A. Riss, M. Parzer, N. Reumann, H. Müller, E. Bauer, S. Khmelevskyi, R. Podloucky, T. Mori, and K. Tobita *et al.*, Boosting the thermoelectric performance of $Fe_2VAl$-type Heusler compounds by band engineering, Phys. Rev. B **103**, 085202 (2021).

[47] N. Reumann, A. Riss, F. Garmroudi, M. Parzer, J. Kovacevic, T. Mori, and E. Bauer, Thermoelectric properties and low-temperature transport anomalies in the $p$-type full-Heusler compounds $Fe_{2-x}Cr_xVAl$, Phys. Rev. B **106**, 235138 (2022).

[48] G. Rogl, F. Garmroudi, A. Riss, X. Yan, J. Sereni, E. Bauer, and P. Rogl, Understanding thermal and electronic transport in high-performance thermoelectric skutterudites, Intermetallics **146**, 107567 (2022).

[49] The valence band at Γ is triply degenerate and the conduction band comprises sixfold generate half-pockets at X, thus, also equaling $N = 3$.

[50] G. J. Snyder, A. H. Snyder, M. Wood, R. Gurunathan, B. H. Snyder, and C. Niu, Weighted mobility, Adv. Mater. **32**, 2001537 (2020).

[51] E. Alleno, Review of the thermoelectric properties in nanostructured $Fe_2VAl$, Metals **8**, 864 (2018).

[52] https://doi.org/10.48436/04ts4-pp738

[53] F. Garmroudi, M. Parzer, A. Riss, A. Pustogow, T. Mori, and E. Bauer, Pivotal role of carrier scattering for semiconductorlike transport in $Fe_2VAl$, Phys. Rev. B **107**, L081108 (2023).

[54] D. I. Bilc, G. Hautier, D. Waroquiers, G.-M. Rignanese, and P. Ghosez, Low-dimensional transport and large thermoelectric power factors in bulk semiconductors by band engineering of highly directional electronic states, Phys. Rev. Lett. **114**, 136601 (2015).

[55] A. Jain, S. P. Ong, G. Hautier, W. Chen, W. D. Richards, S. Dacek, S. Cholia, D. Gunter, D. Skinner, and G. Ceder *et al.*, Commentary: The Materials Project: A materials genome approach to accelerating materials innovation, APL Mater. **1**, 011002 (2013).